# Effects of Erbium Incorporation on Structural, Surface Morphology, and Degradation of Methylene Blue Dye of Magnesium Oxide Nanoparticles

Imene Ameur, Ahmed Reda Khantoul, Boubekeur Boudine, Valérie Brien, David Horwat, Miloud Sebais, Ouahiba Halimi

# Effects of Erbium Incorporation on Structural, Surface Morphology, and Degradation of Methylene Blue Dye of Magnesium Oxide Nanoparticles

Imene Ameur[1*], Ahmed reda Khantoul[2], Boubekeur Boudine[1], Valérie Brien[3], David Horwat[4], Miloud Sebais[1], Ouahiba Halimi[1]

[1] Crystallography Laboratory, Physics Department, Faculty of Exact Sciences, Mentouri Brothers- Constantine 1 University, Route Ain El bey, Constantine 25000, Algeria

[2] Research Center in Industrial Technologies CRTI, P. O. Box 64, Cheraga 16014, Algiers, Algeria

[3] Université de Nantes, CNRS, Institut des Matériaux de Nantes Jean Rouxel, IMN, F-44000 Nantes, France.

[4] Université de Lorraine, CNRS, IJL, F-54000, Nancy, France.

*E-mail: imeneame@yahoo.com

**Abstract**

This paper reports the chemical synthesis of MgO and Er-doped MgO nanoparticles (NPs) by the sol-gel method. Their microstructural, optical characterization and the evaluation of their photocatalytic activity are presented. The synthesized NPs were characterized by means of X-ray diffraction (XRD), Fourier Transform Infrared Spectroscopy (FTIR), Environmental Scanning Electron Microscopy (ESEM), Transmission Electron Microscopy (TEM), Energy Dispersive X-ray Spectroscopy (EDX), UV-visible and Photoluminescence (PL) spectroscopy. The effective synthesis of cubic MgO compound is attested by XRD, FTIR and electron diffraction in TEM. $Er_2O_3$ cubic secondary phase is found in the 2 and 3 wt. % Er-doped MgO samples. The average size of the roundish cuboid-shaped crystallites decreases from 50 nm to 32 nm upon the incorporation of the rare earth element (TEM, XRD). Concomitantly, the size of flakes in which the NPs do agglomerate follows the same trend (ESEM). UV-Visible results show that the calculated band-gap energy of the NPs was in the 5.23 to 5.35 eV range. PL analysis showed that all samples have visible emissions owing to the formation of defects in the MgO band-gap. The photocatalytic activity against methylene blue dye was evaluated under UV light irradiation. The photocatalytic results showed an improvement in degradation efficiency with the addition of erbium in samples, with a

maximal MB dye removal for the 3 wt. % Er-doped MgO sample after 90 min irradiation. The performance is ascribed to a higher separation of the photo-generated (electron-hole) and larger surface area.

**Keywords:** MgO, Erbium, X-ray diffraction, Methylene blue, Photocatalytic activity.

## 1. Introduction

Scientists are concerned about finding solutions to the growing pollution of air and potable water and are notably looking for cost-effective treatments to eliminate organic dissolved dyes from effluents or get rid of $NO_2$ and $CO_2$ in air [1]. Heterogeneous photocatalysis using semiconductor oxides has emerged as one of the effective methods in the degradation of an organic pollutant to clear out various dangerous species from wastewater without any secondary pollution [2, 3]. Through the years, several semiconductor oxides were utilized as efficient photocatalysts, such as: $TiO_2$, ZnO, ZnSe, $WO_3$, $Fe_2O_3$, etc… [4-6].

Among the different metal oxide nanoparticles used for photocatalytic applications, magnesium oxide MgO, which displays a rock-salt structure FCC (NaCl-type) with a lattice parameter of a = 4.21 Å [7], has attracted the attention of researchers. Its large band-gap, its excellent thermodynamic stability, its low refractive index and catalytic properties [8], its pore volume and high possible specific surface areas makes MgO interesting for wide applications. Domains go from catalysis, waste remediation, antibacterial materials, additives in refractory, paint, antifungal to ceramics [9, 10]. MgO has appeared also as an effective candidate in the field of photocatalysis, due to its ability to remove pollutants easily [8]. However, the fast recombination of the electron-hole pairs in MgO is a limiting factor in the photocatalytic degradation process. To overcome such problems, many researchers have tried doping with rare earth elements (La, Gd, Ce and Er) into the MgO lattice by adjusting the structure, size, band-gap energy, or morphology to improve the catalytic performance and some other properties. It is significant to know that the addition of rare earth elements into oxides such as MgO is one of the beneficial strategies that has a hugely positive effect on the application of photocatalytic activity owing to its 4f–5d and 4f–4f electron transition configuration [11, 12]. For example, Shanthi et al. [13] successfully synthesized Gd-doped MgO nanoparticles and studied their photocatalytic activity in the degradation of methylene blue. It has been found that the Gd-doped MgO nanoparticles have a higher methylene blue degradation rate than undoped MgO under UV radiation. Srisuvetha et al. [14] also explored the high photocatalytic activity of Ce-doped MgO. Rare-earth elements into MgO can trap a

photo-induced electron which leads to minimizing the recombination of the electron-hole pairs, enhancing the absorption level, producing few defects, thereby decreasing the band-gap energy and reducing the mean crystalline size [15]. Among all rare earth, erbium (Er) in particular has received much attention as a dopant, owing to its peculiar chemical and physical properties, emissions in the visible region and infrared, suitable infra-f transition and an overlap with the conduction band resulting in the decrease of the band-gap value of host material [16].

The structure and morphology of materials mainly depend upon the synthesis condition and limitations [17]. With regard to the method of preparation, various protocols have been developed for the preparation of pure and doped MgO nanoparticles such as the sol-gel process [18, 19], co-precipitation [20], thermal decomposition [21], chemical vapor deposition [22], Ultrasonic method [23, 24], micro-wave assisted [25], hydrothermal [26] and green synthesis [27, 28]. Herein, the sol-gel route was selected as a synthesis method due to its simplicity and cost effectiveness.

This paper is aiming at presenting a preparation route of MgO and Er-doped MgO NPs using the sol-gel process and at studying the effects of Er dopant with low concentrations (1, 2 and 3 wt. %) on the structural, morphological, optical and photocatalytic properties of MgO NPs. In the literature, only a few studies have reported the photocatalytic degradation of organic pollutants by MgO nanoparticles doped with rare-earth elements, and until now no report could be found studying the effect of Er addition on the properties and photocatalysis applications of MgO NPs using methylene blue dye under UV radiation.

## 2. Experimental

### 2.1 Sol-gel synthesis of MgO and Er-doped MgO NPs

Undoped MgO and Er-doped MgO (Er: 1, 2 and 3 wt. %) NPs were fabricated by a sol-gel route. The precursor species used in the preparation solution were: Magnesium acetate tetra-hydrate Mg $(CH_3COO)_2$. $4H_2O$ (Merck, 99.5% purity) as a magnesium source, Erbium III chloride hexa-hydrate $Cl_3Er$. $6H_2O$ (Aldrich Chemistry, 99.9% purity) as a dopant source, absolute ethanol $C_2H_5OH$ (J. Kollin Chemical, 99.9% purity) as a solvent, and oxalic acid di-hydrate ($C_2H_2O_4$) $2H_2O$ (Merck, 98% purity) as a complexing agent. First, magnesium acetate tetra-hydrate and erbium (III) chloride hexa-hydrate were dissolved in 20 ml of absolute ethanol under magnetic stirring of 1.5 M with [Er] / [Mg] weight ratios of 0, 1, 2 and 3 wt. %. The pH of the solution was then adjusted to pH 5 using 1 M oxalic acid. The solution was kept for 1 h under constant stirring at room temperature until a thick white gel was

formed. The white gel formed was left free overnight before being dried in an oven at 100 °C for 24 h. The dried materials were grounded using a marble mortar and pestle to produce a fine powder. Finally, the fine powders were annealed at 950 °C to form undoped MgO and Er-doped MgO NPs.

### 2.2 Photocatalysis Measurements

The photocatalytic behavior of MgO and Er-doped MgO nanoparticles (Er: 1, 2 and 3 wt. %) was assessed by monitoring the photodegradation of methylene blue (MB) dye under UV irradiation at room temperature. The photodegradation procedure starts with placing 0.20 g nanoparticles synthesized in a Petri dish which contains 50 ml of MB aqueous solution with an initial concentration of about ~ $10^{-5}$ M. Prior to irradiation, solutions were stirred for 30 min in the dark to achieve adsorption/desorption equilibrium between the organic molecules and the catalyst surface. Furthermore, the degradation of MB was also carried out without a catalyst to deduce the light irradiation influence. Then the Petri dish containing the samples and MB dye was irradiated with a 365 nm monochromatic UV-lamp (15 W), which was positioned at a distance of $8 \times 10^{-2}$ m above the surface of the solution. 4 ml was taken out every 10 min from the reactor during irradiation with UV light, in order to enable the recording of absorbance spectra by using UV-3101 PC-Shimadzu double-beam spectrophotometer. The MB concentration was calculated thanks to a calibration curve linking the concentration to the optical absorbance. The percentage degradation of MB can be expressed by the equation below [29, 30]

$$\eta = \left(1 - \frac{c}{c_0}\right) \times 100\%$$

### 2.3 Characterization Techniques

Several methods were utilized to characterize MgO and Er-doped MgO nanoparticles. X-ray diffraction (XRD) was used to perform the structural analysis. The XRD data presented in this paper were obtained with a PANalytical X'Pert diffractometer using the Cu Kα radiation source (λ = 0.1540 nm). The chemical analysis by Fourier transform infrared spectroscopy (FTIR) was performed using a JASCO FTIR – 6300 spectrophotometer. The surface morphology was evaluated by the Environmental scanning electron microscope type (ESEM) XL 30 FEG Philips and Transmission electron microscopy (TEM) using a Philips CM 200 microscope operating at 200 kV voltage. The optical absorption analysis was performed by

using the UV-3101 PC-Shimadzu double-beam spectrophotometer and the PL analysis with a Perkin-Elmer LS 50B spectrophotometer using He-Cd laser.

## 3. Results and Discussion

### 3.1 X-ray Diffraction (XRD) Analysis

XRD diffractograms of undoped and Er-doped MgO (Er: 1, 2 and 3 wt. %) NPs are shown in **figure 1**. The peaks observed at angles 2θ = 36.76, 42.86, 62.24, 74.83, 78.70, 93.97, 105.86 and 109.74 ° appearing in all XRD patterns correspond to the crystalline phase of cubic MgO compound with respective Miller indices (111), (200), (220), (311), (222), (400), (331) and (420) according to (JCPDS card N°. 00-045-0946). Diffractograms of 0 and 1 wt. % sample contains only peaks attributed to MgO, whereas diffractograms of samples prepared with 2 and 3 wt. % contains two families of peaks that could be attributed to MgO and $Er_2O_3$. Indeed, angle positions 2θ = 20.70, 29.34, 33.87, 48.87 and 57.92 ° correspond to (211), (222), (400), (440) and (622) planes of the cubic structure of the $Er_2O_3$ compound (JCPDS card N°. 01-077-0460). The relative intensities of the peaks of the two phases indicate that MgO is in the majority and $Er_2O_3$ is in the minority. **Figure 2** presents a zoom on the region of interest around the most intense peak of MgO for all samples, allowing us to follow the shift of the (200) MgO peak versus the Er doping.

Numerical experimental details of peaks as: angles of peaks, Miller indexations, width at half maximum and corresponding plane distances, extracted from the diffractograms are compiled in table 1. The average size of crystallites D (nm) was grossly estimated from the X-ray diffraction diffractograms by using the Scherrer empirical method. Microstrain ε, and stress σ (GPa) were evaluated from the equations below [31, 32].

$$D = \frac{0.9\lambda}{\beta \cos\theta}$$

$$d_{hkl} = \frac{a}{\sqrt{h^2 + k^2 + l^2}}$$

$$\varepsilon = \frac{\beta \cos\theta}{4}$$

$$\sigma = \varepsilon E$$

Where λ, β, θ, and E are the X-ray wavelength (1.5402 Å), full width at half maximum $F_{WHM}$ in radians, Bragg's diffraction angle, and Young's modulus of MgO~ 300 GPa, respectively. The calculated values of D (nm), ε, σ (GPa) and a (Å), are also listed in **table 1**.

Noticeably, when 1 and 2 wt. % Er is used in the precursor solution, (200) MgO peak shift towards lower angles. However, for 3 wt. % Er, this peak (200) slightly shifts towards higher diffraction angles. For all samples, the lattice parameter a (Å) of MgO lattice was calculated (refer to table 1). As observed also, a decrease in the intensity of MgO diffraction peaks when Er doping is added, which may cause a distortion in the lattice and deteriorate the crystal structure of MgO.

The MgO lattice of the Er-doped MgO sample prepared at 1 wt. % exhibit a 0.07 % increase, potentially attesting of a crystallographic incorporation of the Erbium dopant ions in cubic MgO crystal. This expansion is still slightly present (+0.02 %) for the Er-doped MgO sample prepared at 2 wt. %, but is nil for the sample prepared at 3 wt. %, when the secondary oxide phase is formed.

Such an increase in parameter a (Å) of MgO cell (for 1 wt. % and at 2 wt. %) may be the signature of successful incorporation of the lanthanide ion in MgO and might be attributable to the larger atomic radius of Er compared to that of Mg. Interestingly, this shift is less pronounced when the second phase appears (from 1 to 2 Er wt. %), to become undetectable at 3 % of Er. We then suppose that the metal enter the MgO lattice (maximized for 1 % of Er in the precursor solution), but this incorporation is reduced (from 2% Er and above in the precursor solution) when the metal can form its oxide. This assumption could be corroborated by the estimated values of stress. They increase from 0.24 GPa in pure MgO to 0.35 GPa for the sample prepared from 1% of Er in the precursor solution then reduce to around 0.30 GPa for the higher concentrations.

It can be seen that all non-doped and Er-doped MgO crystallites have a nanometric size laying in the 32.2–49 nm range. It is worth also noting that the average size of crystallites decreases when Er is added. The incorporation of larger Er ions in the host MgO lattice minimizes the nucleation and the growth rate of MgO crystals; this may be the reason behind the reduction in crystallite size with Er doping. It roughly corresponds to an increase of 50 percent in the surface to volume ratio. Therefore the specific surface area increases significantly, which is a key positive factor regarding catalytic applications.

### 3.2 Fourier Transform Infrared (FTIR) Analysis

**Figure 3** shows the Fourier transform infrared (FTIR) spectra of the synthesized undoped MgO and Er-doped MgO NPs. They were carried out in the spectral range frequencies going from 500 to 3500 $cm^{-1}$. The peaks noticed on the spectra match with the vibration modes correlating to the Mg–O, O–H bonds and the bonds in the MgO. This was obtained when comparing our spectra with spectra from the literature. The peaks measured at 861 and 989 $cm^{-1}$ can be attributed to the stretching vibration modes of Mg–O–Mg bonding [33], the peaks observed at 1421, 1517, and 1661 $cm^{-1}$ were ascribed to the vibration modes in the hydroxyl group [34], the peak located at 2356 $cm^{-1}$ was attributed to the absorption of atmospheric gas phase $CO_2$ [32], and the band at 2922 $cm^{-1}$ may correspond to the O–H group in the synthesized products from ethanol or water absorbed during the product elaboration [34].

As we know, when the MgO surface is exposed to the atmosphere, $CO_2$ and $H_2O$ molecules are easily chemisorbed. This data is highlighting that samples elaborated with 1 and 2 wt. % possess a similar vibrational response, reinforcing the hypothesis assumed in XRD analysis, which is that MgO crystals of MgO:Er (2 wt. %) and MgO:Er (1 wt. %) samples contain erbium ions. On the other hand, the 3% sample exhibits a vibrational signal resembling that of pure MgO, indicating they share a similar structure which can be identified as MgO with little or no erbium.

### 3.3 Environmental Scanning Electron Microscopy (ESEM) Analysis

Surface morphology was observed by environmental scanning electron microscopy (ESEM). The ESEM micrographs of undoped and Er-doped MgO (1, 2 and 3 wt. % Er) NPs obtained by the sol-gel route are shown in **figure 4**.

All samples undoped and Er-doped MgO look alike. There are constituted by big agglomerated grains and smaller bits. The big grains measure 100-300 μm whereas the small bits or flakes lay in the 1-10 μm range. One will note that the granularity of the samples offers a high level of porosity, which implies a high specific surface in case of activity which may be advantageous for photocatalytic activity.

### 3.4 Transmission Electron Microscopy (TEM) Analysis

Transmission electron microscopy (TEM) was used to reveal the fine morphology as the size of the grains, and confirm their crystallographic structure. **Figure 5** shows TEM micrographs of undoped MgO and Er-doped MgO NPs. All samples exhibit common features. Samples

are made of roundish cuboid-shaped grains aggregating in a substantial manner. The size and the distribution of the particles were measured and are detailed further. Similar morphology was found by Anilkumar et al. [8] for MgO nanopowder synthesized by the green mediated. route.

**Figure 6** shows selected area electron diffraction (SAED) patterns of undoped MgO and Er-doped MgO NPs. The SAED patterns are composed of a set of dotted rings confirming the good crystallinity and the polycrystalline character of the prepared nanoparticles (see fig 6). The observed rings have been indexed with the MgO (JCPDS card N$^{o}$ 00-045-0946), inflating the rings by a coefficient up to 0.06 % accordingly with precedent XRD results. SAED pattern of sample 2 % also seem to contain some spots that might be the ones of $Er_2O_3$ (see arrow of fig 6 c). **Figure 7** shows grain size distributions histogram of undoped and Er-doped MgO NPs derived from TEM analysis.

The average grain size D was calculated from TEM micrographs by using ImageJ software and is reported in **table 2**. Exactly like what was observed after analyzing the width of XRD peaks, D slightly decreases with Er doping increase, and the values lay between 40-50 nm. A larger grains size is observed in TEM compared to that derived from XRD data. This is likely due to the agglomeration of some crystallites, as can be seen in the bright field TEM images. It can be remarked that the size of flakes in which the NPs agglomerate and that were observed by ESEM follows the diminishing of the crystallites size measured here. The decrease in these two features versus erbium content leads to an increase of the surface area of samples. This is a significant factor to enhance photocatalytic activity.

### 3.5 Energy Dispersive X-ray Spectroscopy (EDX) Analysis

The elemental composition of the nanoparticles was investigated by energy-dispersive X-ray spectroscopy (EDX) on the TEM CM20 Philips microscope equipped with an ultra-thin detector to perform EDX. **Figure 8** presents EDX signals of undoped MgO and Er-doped MgO (Er: 1, 2 and 3 wt. %) NPs prepared by the sol-gel route.

EDX spectra reveal the presence of the peaks characteristic of the O-K, Mg-K, Er-L transitions corresponding to nanoparticles constituents and Cu-K transition corresponding to the carbon film-coated copper grid used for the TEM observations. As expected, the 0 % sample does not exhibit the Er peak, whereas high intensities of the Mg and O peaks confirm that the samples are primarily composed of MgO.

**Table 3** gives the semi-quantitative analysis of EDX measurements of the four samples. The relative intensities of Mg, O, and Er peaks demonstrate that the erbium content in the powder can be controlled by the sol-gel route. Indeed, the sample containing 1, 2 and 3 nominal wt. % Er in the precursor solutions was measured to be 1.18, 3.70 and 6.12 wt. % by EDX, respectively.

### 3.6 UV-Visible analysis

Spectrophotometry is a quantitative measurement of the absorption/ transmission or reflection of a material as a function of wavelength. For the samples that we developed, the optical transmittance measurements were carried out at room temperature in the spectral range extending from 200 to 800 nm. The absorption spectra of undoped and Er-doped MgO (1, 2 and 3 wt. %) NPs are reported in **figure 9**.

It was observed that all nanoparticles are almost transparent in the visible region and show strong absorption in the UV region. The absorption threshold located in the ultraviolet range around $\lambda \sim 200$ nm indicates that MgO NPs have a wide optical band-gap. Furthermore, the absorption edge slightly shifted towards the higher wavelength (red-shifted) due to the Er doping, this proves that the Er was successfully doped.

To calculate the band-gap energy of our samples from the absorption spectra, and because MgO is a direct band-gap semiconductor, the Tauc formula was used [35-37]. When $(\alpha h\nu)^2 = 0$, $Eg = h\nu$, an extrapolation of the linear region of the plot of $(\alpha h\nu)^2$ versus photon energy ($h\nu$) on the x-axis gives the value of the band-gap energy Eg. **Figure 10** shows the extrapolation of the curves $(\alpha h\nu)^2$ as a function of the photon energy ($h\nu$). The calculated values of the band-gap energy of undoped MgO and Er-doped MgO NPs are depicted in **table 2**. The addition of Er into MgO did not significantly change the band-gap value, despite a possible slight decrease with 1 wt. % Er. Overall the band-gap was in the 5.23 to 5.35 eV range.

### 3.7 Photoluminescence analysis

Useful information about the charge carrier's recombination, trapping, crystal and surface defects, etc. can be determined by photoluminescence spectroscopy (PL). The photoluminescence spectra for undoped and Er-doped MgO (Er: 1, 2 and 3 wt. %) NPs at room temperature under the same condition with excitation radiation $\lambda = 488$ nm are shown in **figure 11**.

The visible emissions peaking attributed to the presence of green emission at ~ 534 nm, red emission at ~ 664-764 nm, and red-purple emission at ~ 800 nm. The visible region is relevant to the structural defects such as oxygen vacancies (VO) (F centers) and deep level emissions such as magnesium vacancies (VMg), oxygen interstitials (Oi), and magnesium interstitials (Mgi) [8]. The spectral shape is similar to reported in the literature. Additionally, the overall PL intensity increases with Er doping increased from 1 to 3 %, which indicates Er doping promotes the introduction of defects inside the band-gap. We expect it to play a significant role in the improvement of photocatalytic activity.

### 3.8 Photocatalytic Activity of MgO and Er-doped MgO NPs

The photocatalytic activity of undoped and Er-doped MgO (Er: 1, 2 and 3 wt. %) NPs were evaluated through the degradation of methylene blue (MB) dye under UV irradiation. 0.20 g of nanoparticles synthesized was added to 50 ml of MB aqueous solution with a primary concentration of about ~ $10^{-5}$ M in a Petri dish under magnetic stirring; the obtained solution remained in the dark for 30 min before starting irradiation with UV light. The principle of the evaluation consists in following the evolution of the optical absorption of the solution for different intervals of time and as a function of wavelength from 400 to 800 nm. **Figure 12** shows the UV-Vis absorption spectra of the aqueous MB solution in the presence of MgO and 1, 2, 3 wt. % Er-doped MgO NPs in dark for 30 min and under exposure to UV irradiation. The spectra under UV irradiation were recorded every 10 min until 90 min. To account for the temporal variation of MB dye concentration the maximum absorbance at 664 nm was selected. The intensity of the absorption peak of MB at 664 nm decreases with an increase in the irradiation time, which indicates the degradation of MB dye by photocatalysis.

The absorbance of the solution can be related to the concentration ratio ($C/C_0$) of MB dye and was computed for the four samples versus the irradiation time (resulting graphs are given in **figure 13**. The percentage degradation ($\eta$) of MB in the solutions versus time was then deduced and is given in **figure 14**. Different observations can then be done. No frank degradation of MB could be noticed in the absence of NPs under UV irradiation (reference in black in figure 13 and figure 14). The slight diminution of MB concentration measured is due to the photolysis of MB in water. It is observed that MB is degraded as soon as (doped or undoped) MgO is set in the solution. These observations allow to exclude the effect of UV rays on the MB degradation observed here. After 90 min, $\eta$ of undoped MgO is 93 % whereas 3 wt. % Er-doped MgO is 99 %. The addition of erbium is then having a very positive effect.

When looking closer, one can also realize that the dynamics of MB degradation is differentiated according to the erbium content. The highest MB degradation rate is measured for the 2 and 3 wt. % Er-doped MgO NPs.

In chemical reactions requiring a catalyst, the morphology, the size of the active surfaces, gap energy, and radicals are key parameters playing a major role to monitor their efficiency. During the photocatalytic process, the absorption of photons by the photocatalysts allows electrons from the valence band (VB) to move to the conduction band (CB) and leaves behind a hole in the VB. After that, the photo-generated electron-hole pairs stimulate the oxidation and reduction operation on the surface of the photocatalysts. The band-gap of MgO and Er-doped MgO is much larger than the UV illumination energy. Our hypothesis is that photocatalysis was stimulated by the increased presence of various defects introduced inside the band-gap before and upon Er incorporation and contributed to transitions from these defects that produce energy states inside the band-gap. The generation of defect states in the band-gap permits to reduce the recombination rate of photo-generated electron-hole pairs due to charge transitions happening through defects; this was earlier presented in references [38-40].

Furthermore, we propose that in the presence of water and oxygen, radical species such as •OH, $H_2O_2$, or $\bullet O_2^-$ are generated due to defects existing in MgO (according to PL results), and then attack the organic molecule absorbed on the surface of the catalyst. This leads to the cleavage of bonds within the MB molecule and contributes to the decomposition of MB molecules. Mageshwari et al. [41] informed that radical species might be generated owing to native defects in MgO nanoparticles synthesized by the template-free method. Er-doped MgO would increase surface defects, which can promote photocatalytic efficiency. Er ions can reduce electron-hole recombination. The photo-generated hole on the surface of the catalyst goes through charge transfer with the adsorbed water molecules to produce the active hydroxyl radical •OH. Further, the reduction of molecular $O_2$ by the photo-generated electron results in the reproduction of the $\bullet O_2^-$ radicals, as demonstrated by the reaction process below:

$$Er/MgO + h\nu \rightarrow Er/MgO\ (e^- + h^+)$$

$$h^+ + H^- \rightarrow \bullet OH$$

$$h^+ + H_2O \rightarrow \bullet OH + H^+$$

$$e^- + O_2 \rightarrow \bullet O_2^-$$

$$H^+ + \bullet O_2^- \rightarrow H_2O$$

$$e^- + \bullet O_2^- + 2H^+ \rightarrow H_2O_2$$

$e^- + H_2O_2 \rightarrow \bullet OH + OH^-$

$\bullet O_2^- + H_2O_2 \rightarrow \bullet OH + OH^- + O_2$

$\bullet O_2^- + H^+ \rightarrow \bullet OH_2$

$e^- + \bullet OH_2 \rightarrow HO_2^-$

$HO_2^- + H^+ \rightarrow H_2O_2$

$2\bullet OH_2 \rightarrow O_2 + H_2O_2$

$½\ O_2 + 2H^+ + 2e^- \rightarrow H_2O$

$\bullet OH + MB \rightarrow CO_2 + H_2O$

It is clear that a decrease in crystallite size of Er-doped MgO NPs improves the surface-area-to-volume ratio of the catalysts thereby increasing the number of reactive sites and surface hydroxyl [42]. It results that a higher surface-area-to-volume ratio facilitates the reaction-interaction between the photocatalyst and the dye molecules, which leads to increasing the degradation efficiency [43]. Here the samples that seem to exhibit the highest surface-area-to-volume ratios (see ESEM images in **figure 4**) are also the 2 and 3 wt. % Er-doped MgO NPs.

**Table 4** shows a literature overview of MgO photocatalyst doped with different elements (transition metals and rare earth) for the degradation of organic pollutants from water. In references [44, 45] transition metals (Fe and Ag) were used to dope MgO nanoparticles in order to improve the degradation of MB under UV light of MgO. The results showed that the 4 mol.% Fe and 2 mol.% Ag MgO NPs have achieved 88% and 75% degradation rates, respectively. Furthermore, in works [13, 14] MgO was doped with rare earth elements (Gd and Ce) for the degradation of pollutants (MB, phenol, CR) under UV light in order also to improve the MgO degradation rate. The studies report on a better improvement in degradation rate (between 85-95%) using rare earths than transition metals.
In the present work, MgO and Er-doped MgO NPs were prepared by the sol-gel route. The photocatalytic performance of the Er-doped MgO NPs under UV light reported in the present study reaches 99% (**table 4**).

## 4. Conclusion

In brief, undoped MgO and Er-doped MgO (Er: 1, 2, and 3 wt. %) nanoparticles samples were prepared successfully by the chemical sol-gel method. The crystalline structure of NPs was checked by XRD, which confirms the cubic structure of MgO NPs and the appearance of the $Er_2O_3$ secondary phase, the average mean crystallite size decreases when the Er doping is

incorporated in the MgO lattice. FTIR measurements of the fabricated nanoparticles show the formation of MgO with the characteristic vibrational mode of Mg–O. The surface morphology of NPs through ESEM and TEM images revealed an agglomeration of nanoparticles with rounded shapes. The elemental composition has been carried out by EDX and the spectra reveal that no traces of other elements are found confirming the purity of the samples. UV-Visible indicated that Er addition did not significantly change the band-gap value, the band-gap of NPs was in the 5.23 to 5.35 eV range. The formation of defects in the band-gap of MgO was confirmed by PL analysis. Finally, MgO and Er-doped MgO NPs were used for the removal of MB dye from water and showed that the removal efficiency of dyes increases as the concentration of Er increases, more particularly for short irradiation times. The maximum MB dye removal was 99 % for 3 wt. % Er-doped MgO NPs. Overall; the photocatalytic study showed that the addition of Er dopant to MgO NPs has promoted photocatalytic properties, due to multiple factors such as surface area and less (electron-hole) recombination rate which are important factors that improves the photocatalytic activity.

**Acknowledgements**

We want to thank Mr Badis Rahal and Mrs Sylvie Migot for the help in XRD, ESEM, TEM and EDX measurements.

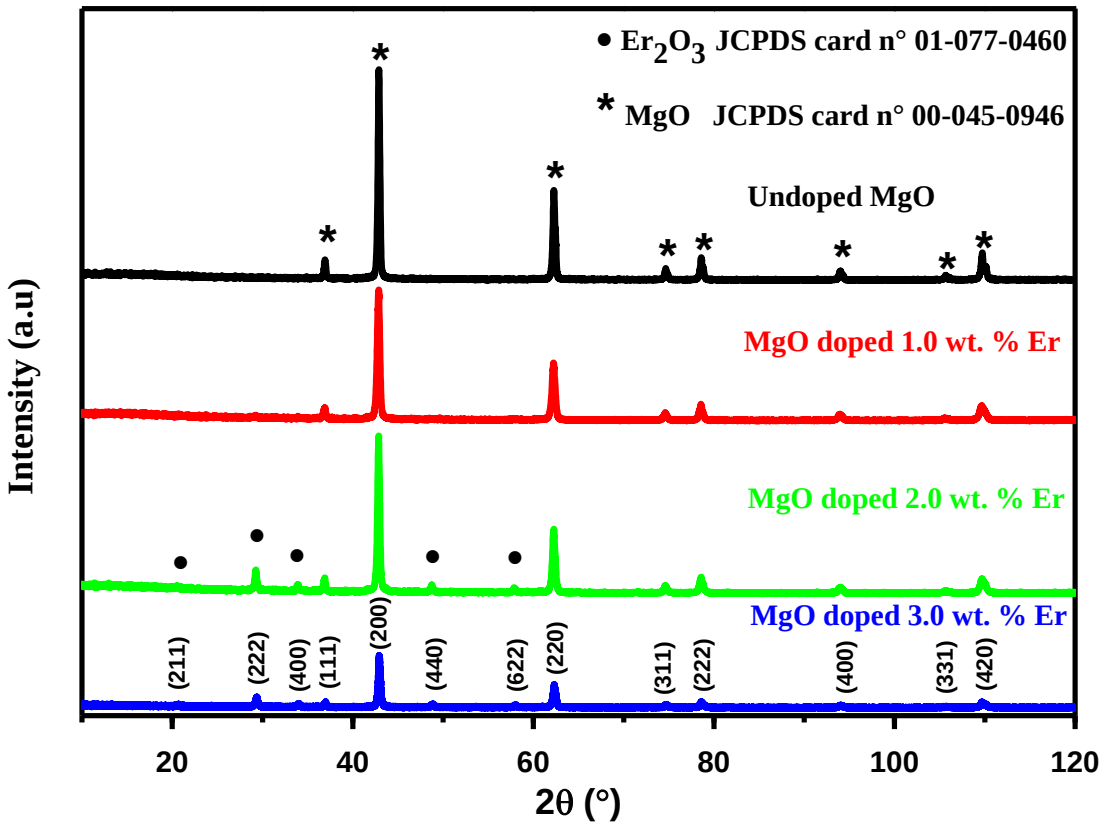


**Fig. 1** X-ray diffractograms of undoped and Er-doped MgO (Er: 1, 2 and 3 wt. %) NPs.

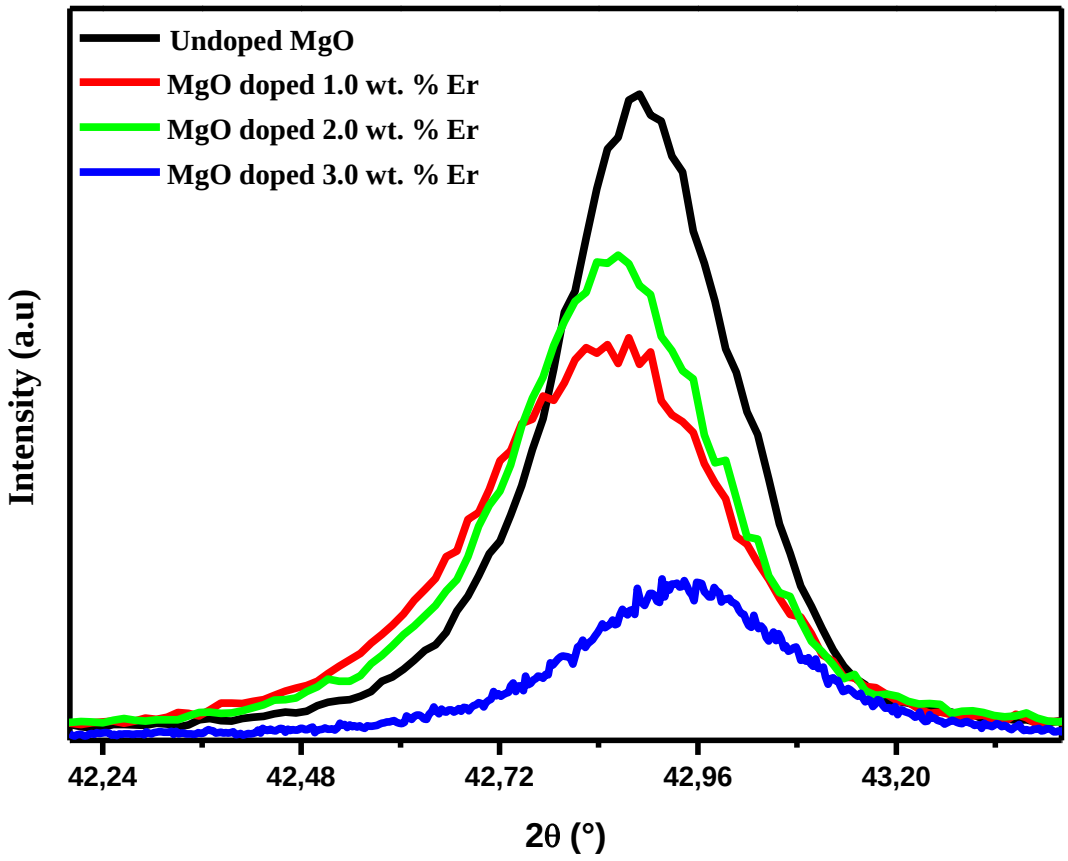


**Fig. 2** Region of interest in the X-ray diffractograms of figure 1 around the intense peak (200) of undoped and Er-doped MgO (Er: 1, 2 and 3 wt. %) NPs.

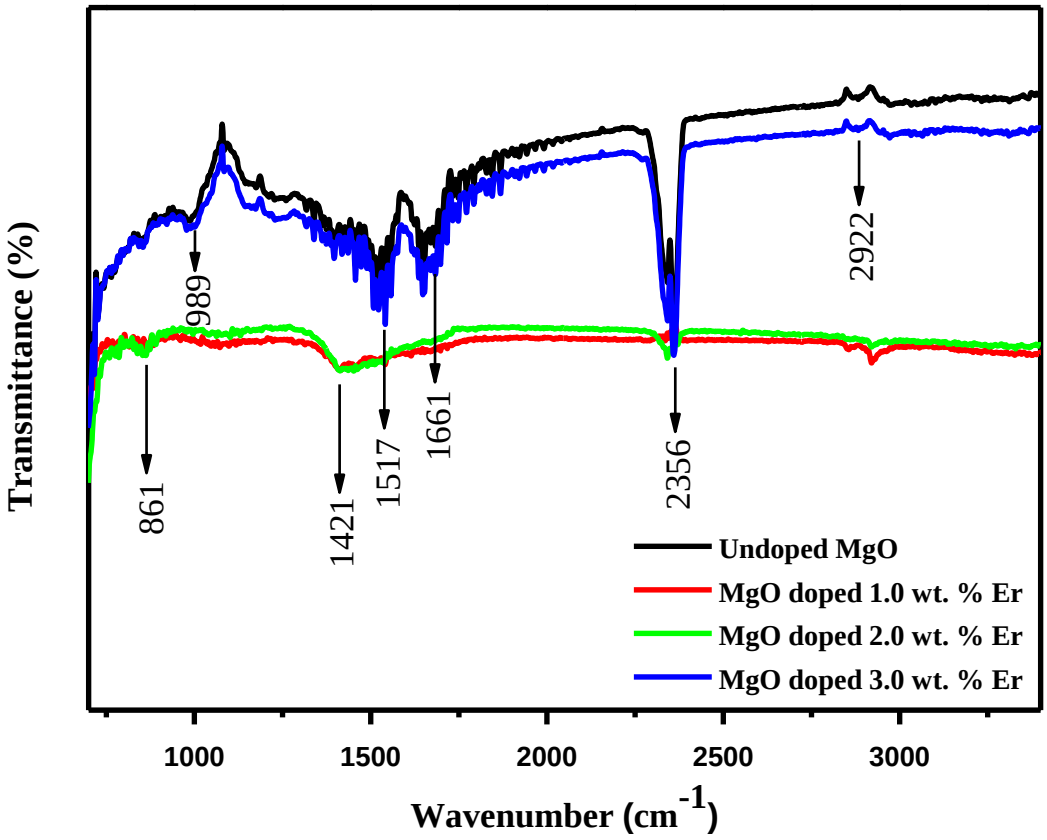


**Fig. 3** FTIR spectra of undoped and Er-doped MgO (Er: 1, 2 and 3 wt. %) NPs.

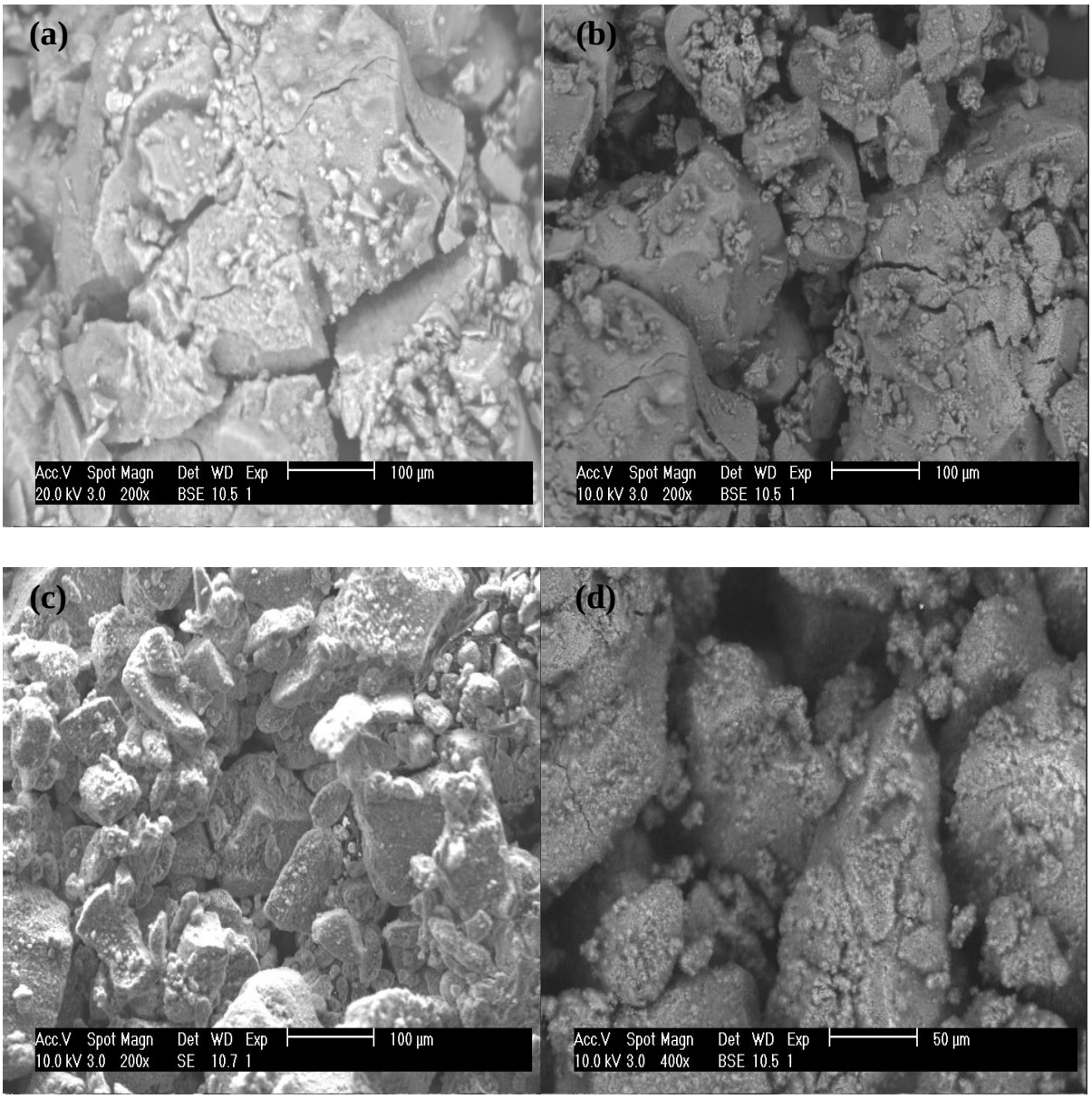


**Fig. 4** ESEM images of undoped MgO and Er-doped MgO NPs: (a) Er 0 wt. %, (b) Er 1 wt. %, (c) Er 2 wt. %, (d) Er 3 wt. %.

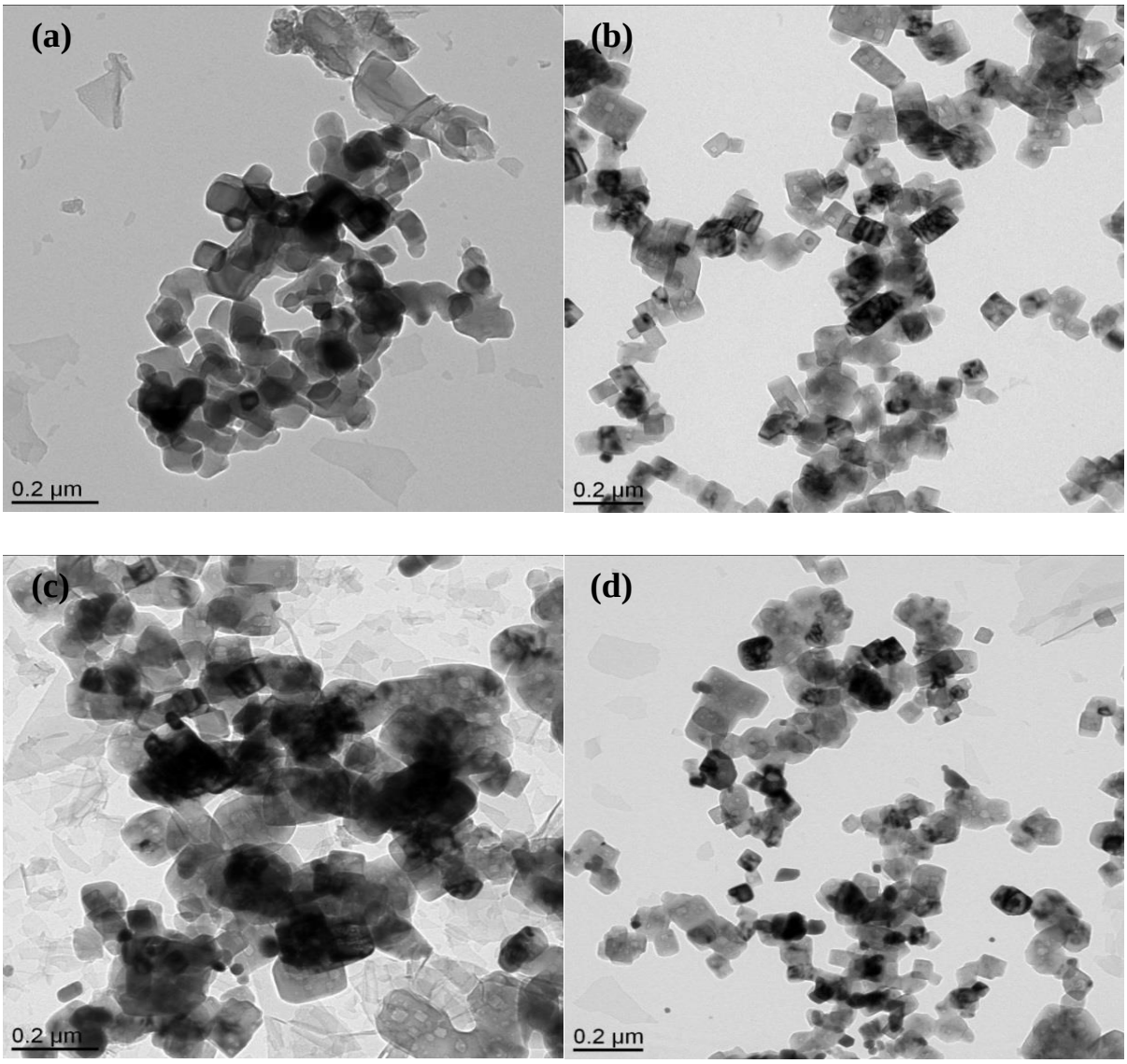


**Fig. 5** TEM micrographs of undoped MgO and Er-doped MgO NPs: (a) Er 0 wt. %, (b) Er 1 wt. %, (c) Er 2 wt. %, (d) Er 3 wt. %.

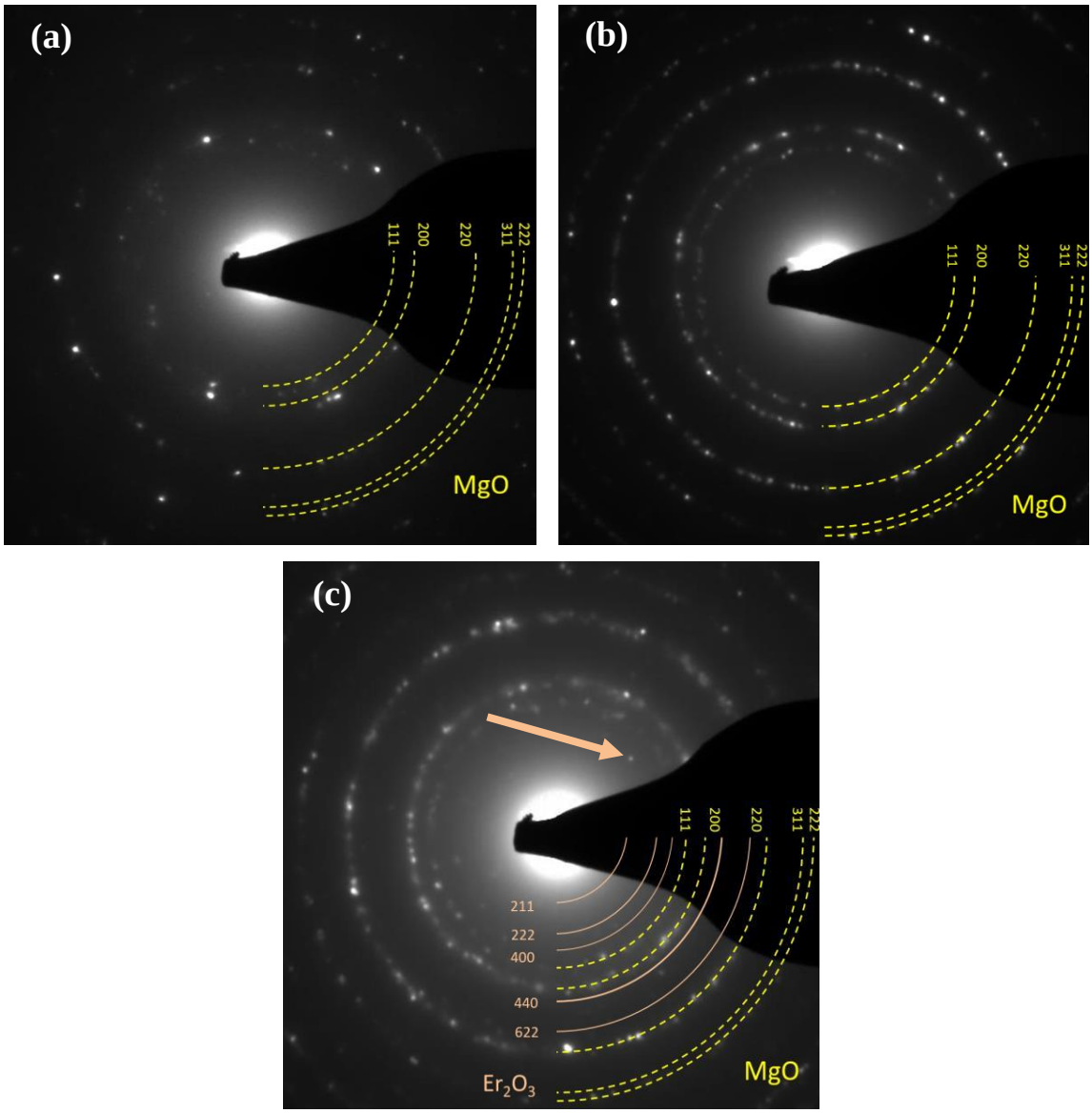


**Fig. 6** SAED patterns of undoped MgO and Er-doped MgO NPs : (a) Er 0 wt. %, (b) Er 1 wt. %, (c) Er 2 wt. %.

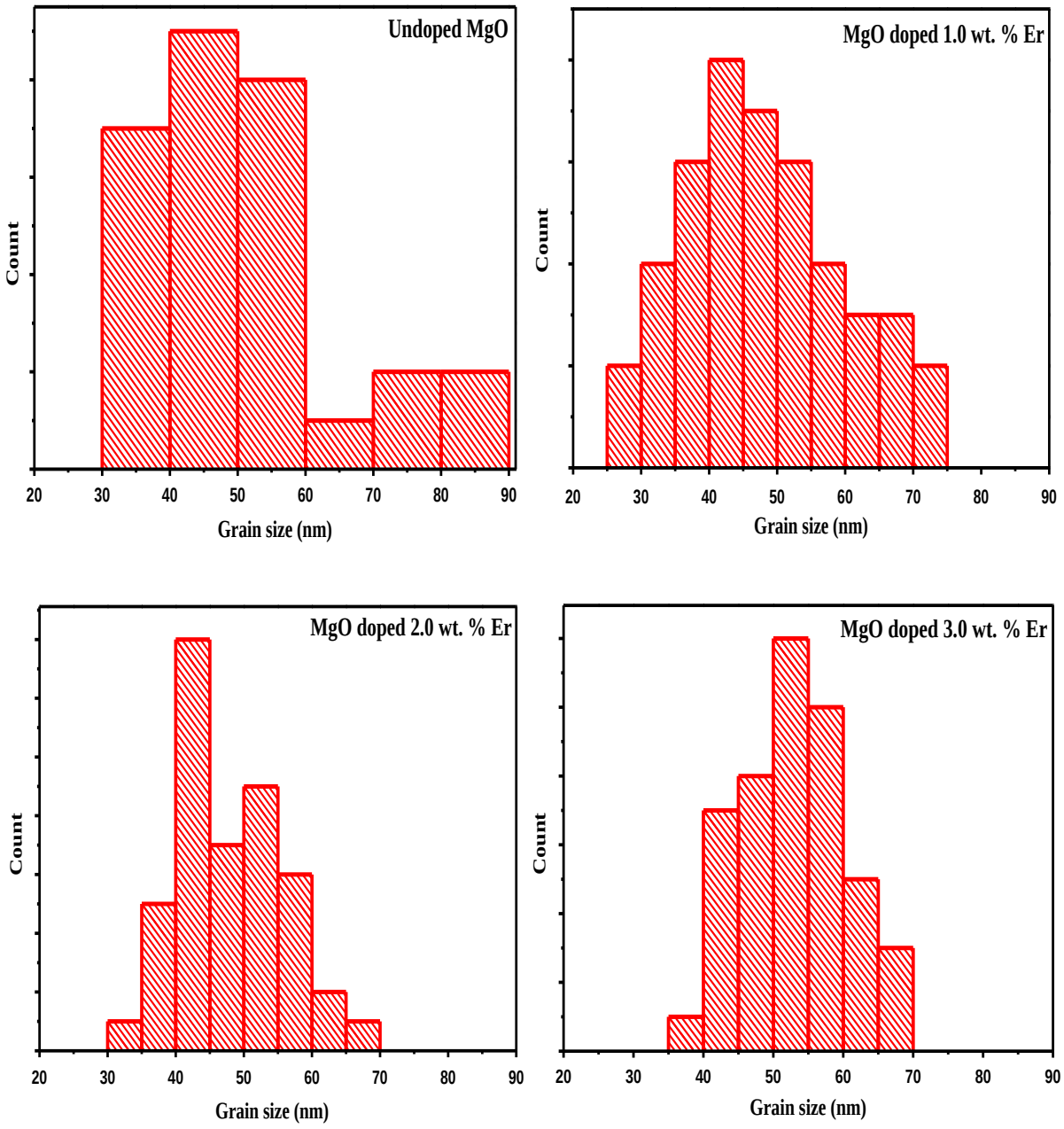


**Fig. 7** Grains size distribution histograms of undoped and Er-doped MgO NPs.

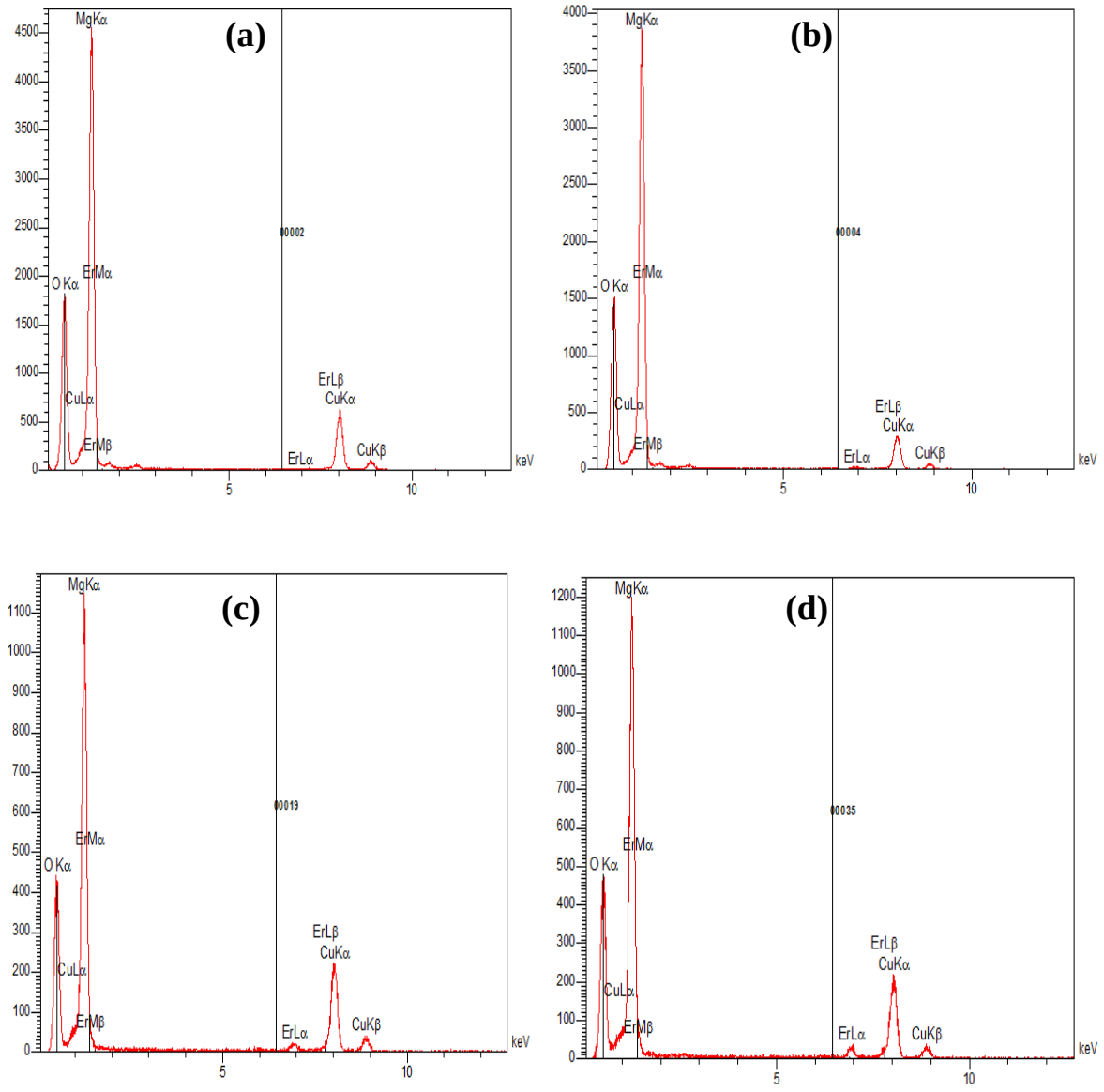


**Fig. 8** EDX spectra of undoped MgO and Er-doped MgO NPs: (a) Er 0 wt. %, (b) Er 1 wt. %, (c) Er 2 wt. %, (d) Er 3 wt. %.

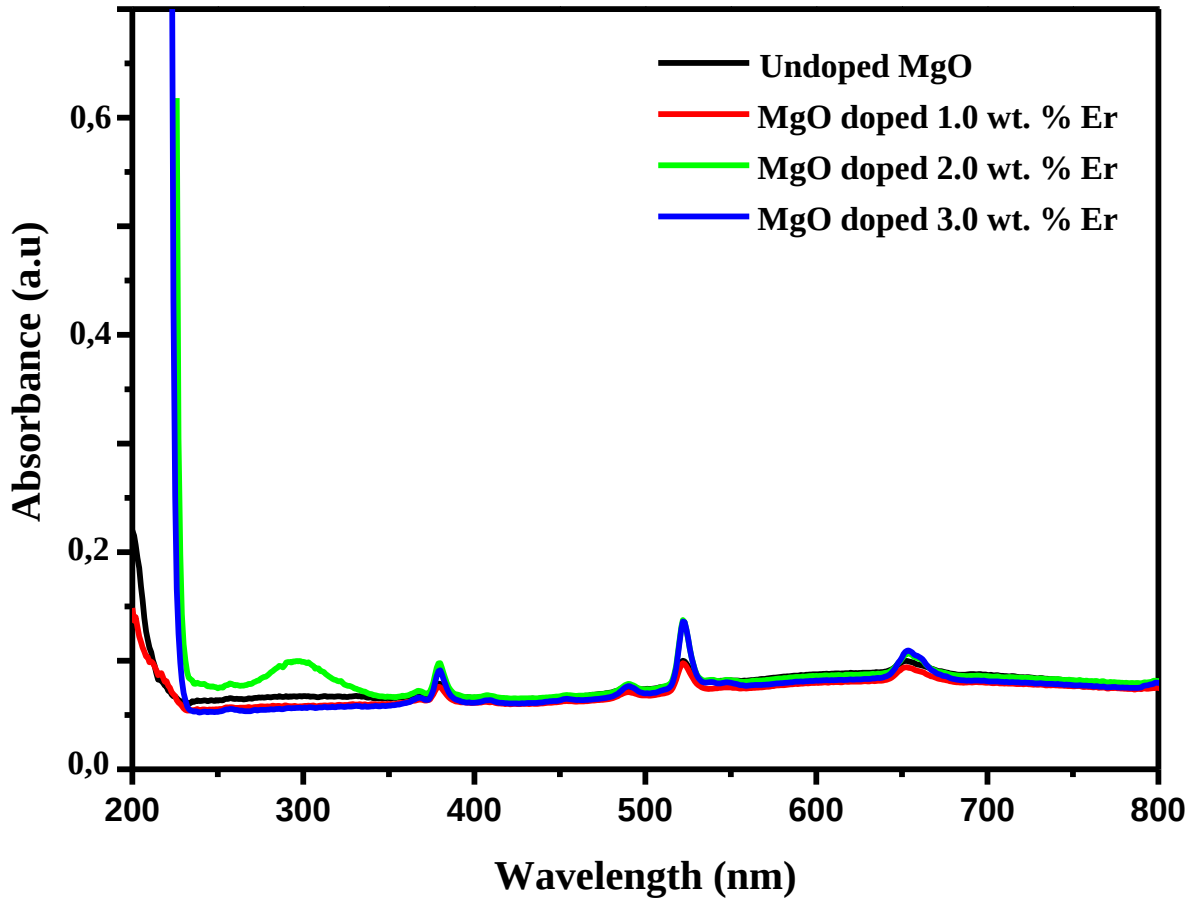


**Fig. 9** Absorption spectra of undoped and Er-doped MgO (1, 2, and 3 wt. %) NPs.

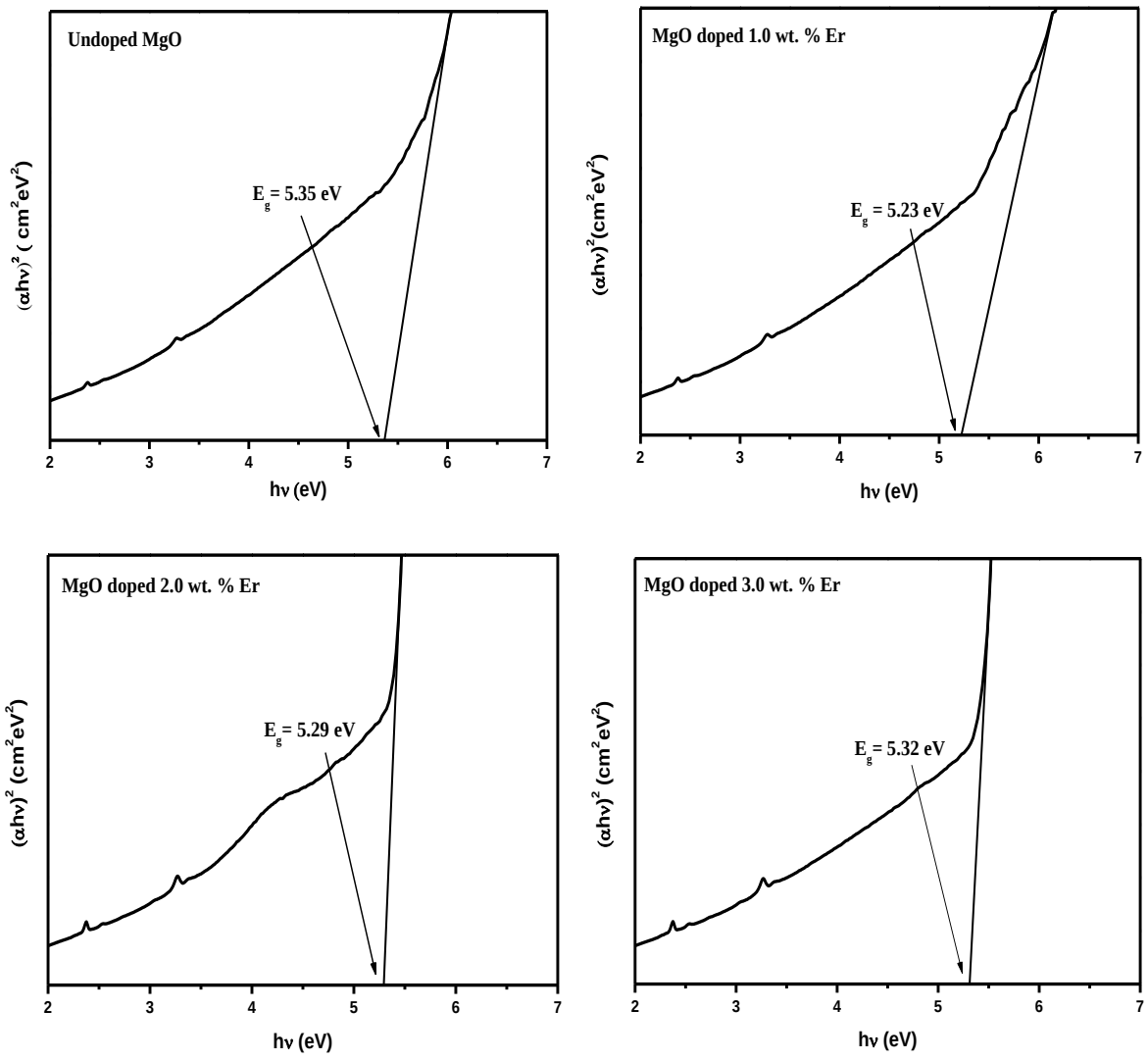


**Fig. 10** The extrapolation of the curves $(\alpha h\nu)^2$ as a function of the photon energy $(h\nu)$ spectra of undoped and Er-doped MgO (1, 2, and 3 wt. %) NPs

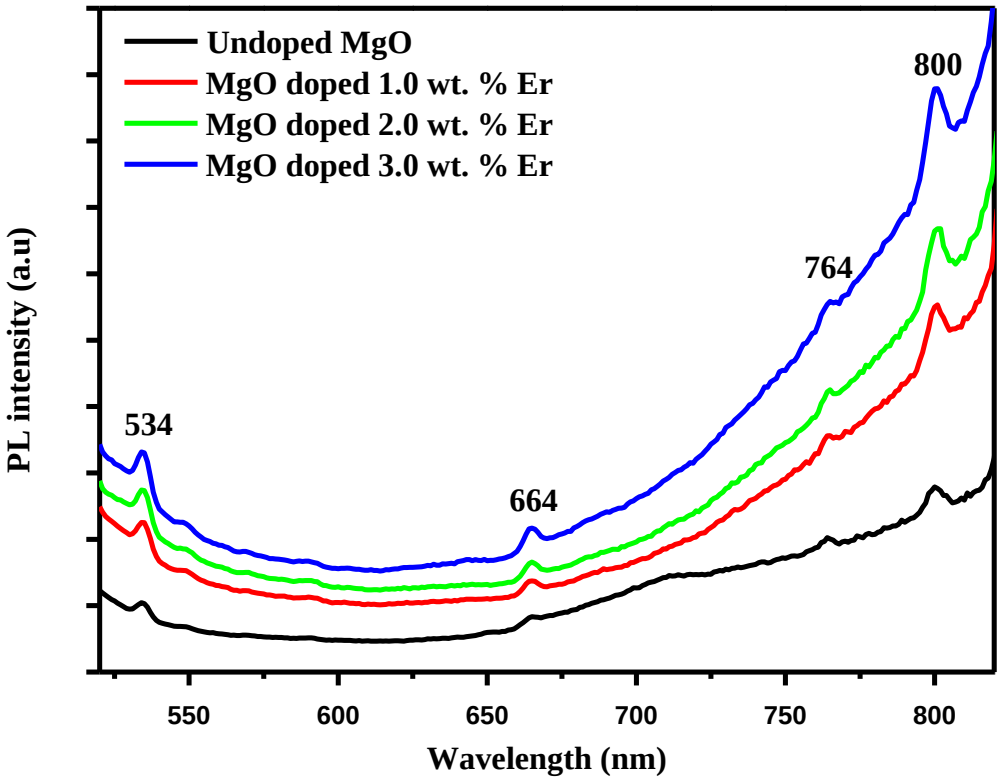


**Fig. 11** Photoluminescence spectra of undoped and Er-doped MgO (1, 2, and 3 wt. %) NPs

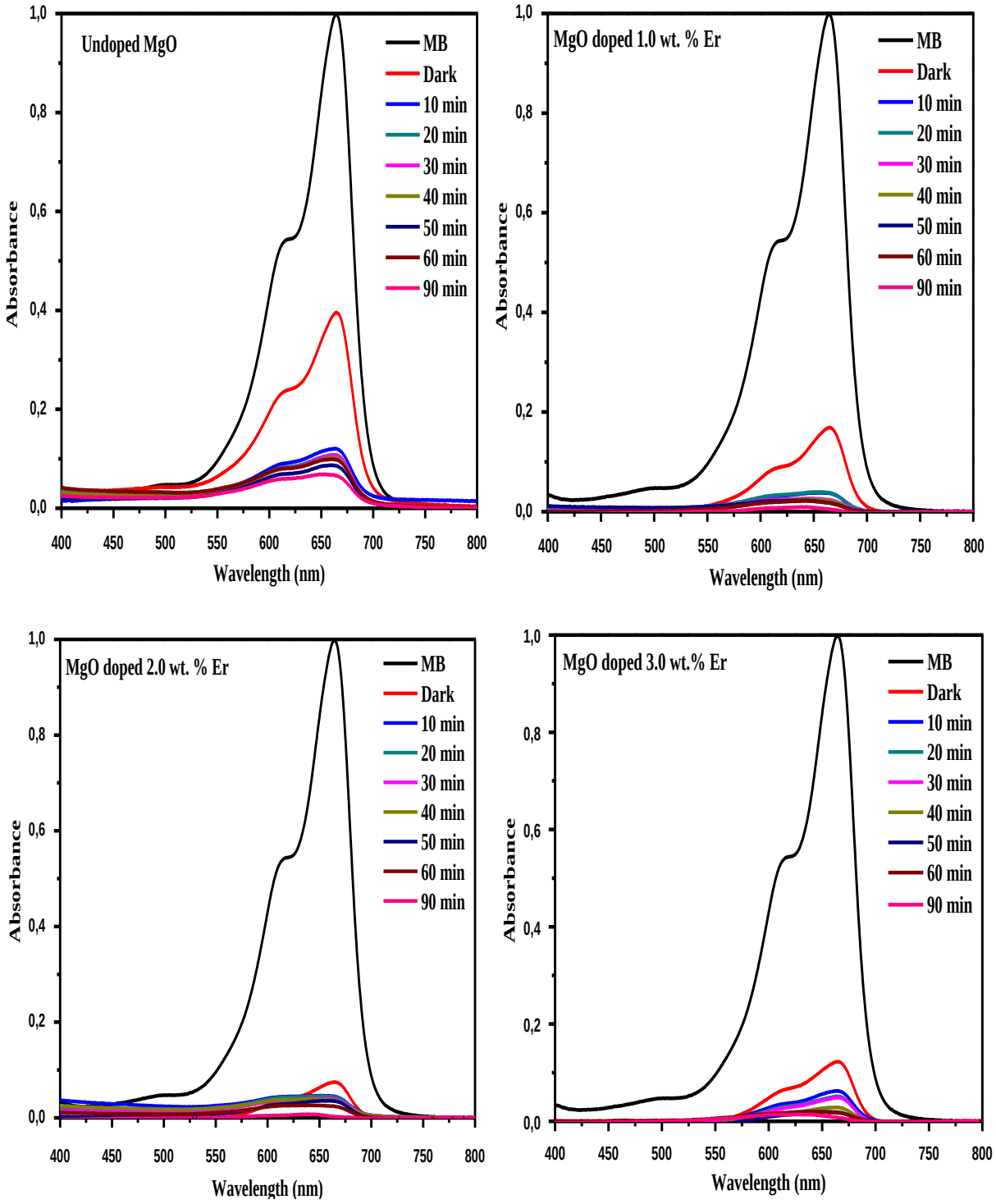


**Fig. 12** Absorption spectra of MB aqueous solution under UV irradiation of undoped and Er-doped MgO (Er: 1, 2, and 3 wt. %) NPs.

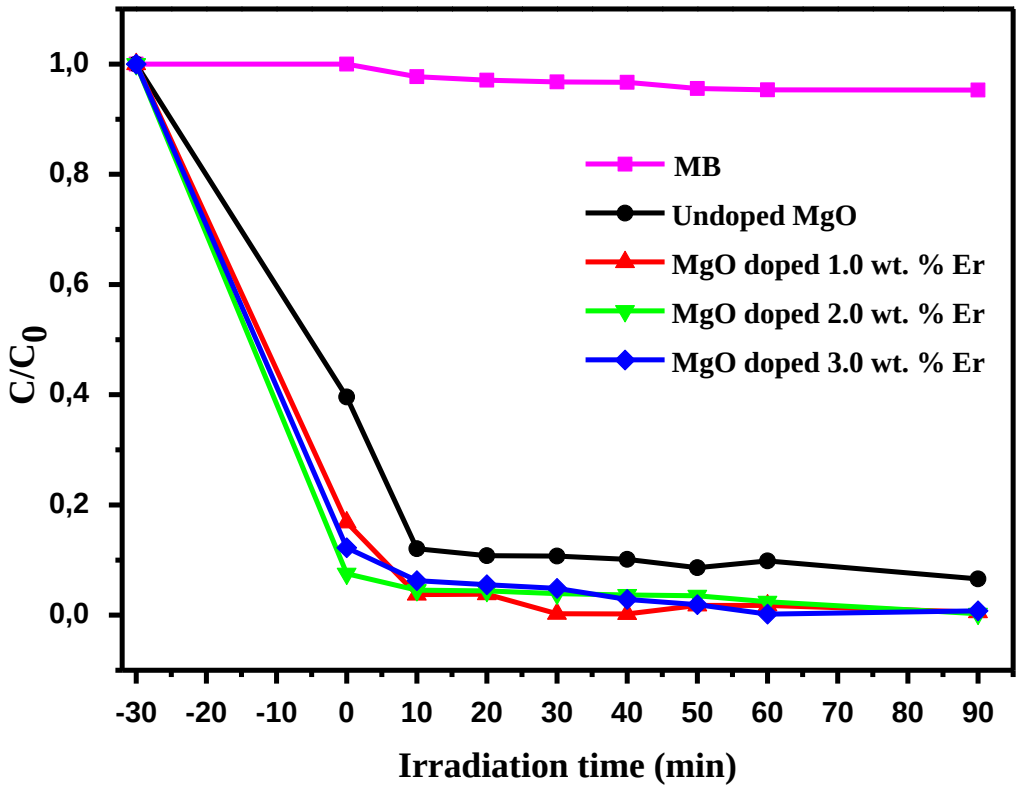


**Fig. 13** $C/C_0$vs irradiation time of undoped and Er-doped MgO (Er: 1, 2, and 3 wt. %) NPs.

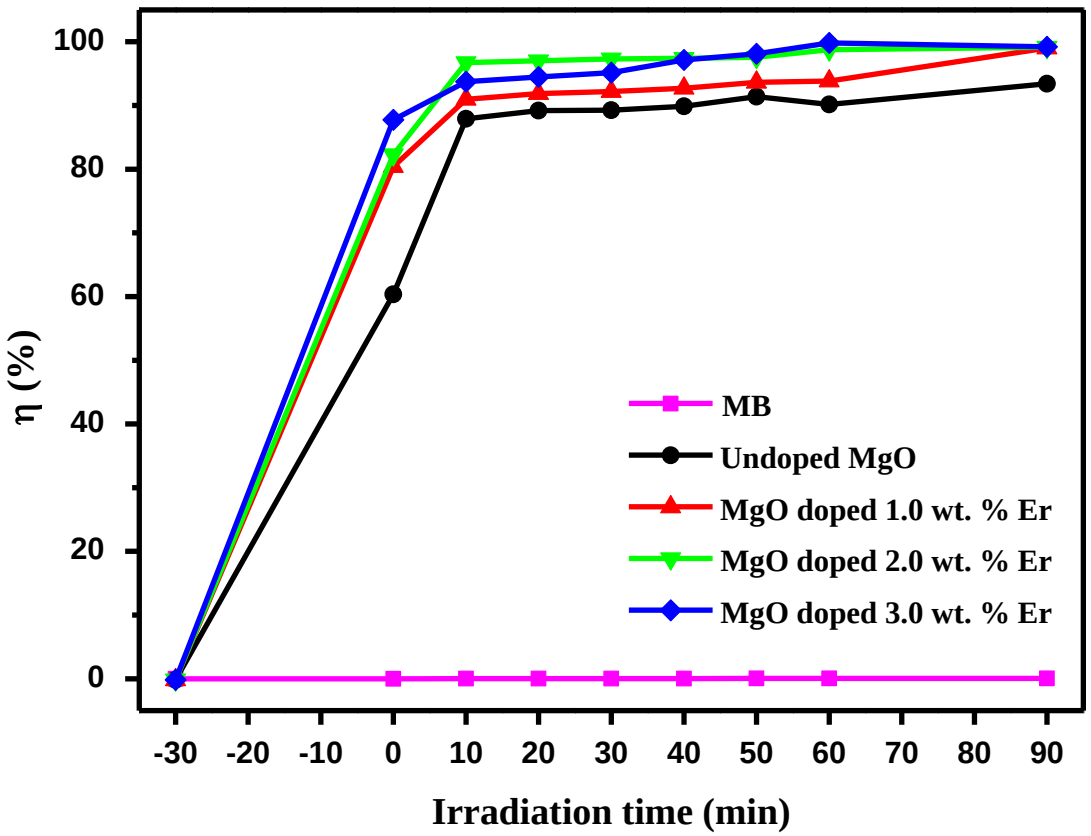


**Fig. 14** Percentage degradation of undoped and Er-doped MgO (Er: 1, 2, and 3 wt. %) NPs.

**Table 1** Structural parameters of the most intense peaks of MgO:(200) and $Er_2O_{3:}$ (222)

| Er % | Phase | 2θ (°) | (hkl) | β (°) | $d_{hkl}$(Å) | D (nm) | ε ×$10^{-4}$ | σ (GPa) | a (Å) |
|---|---|---|---|---|---|---|---|---|---|
| 0 | MgO | 42.86 | 200 | 0.20 | 2.11 | 49.0 | 8.11 | 0.24 | 4.213 |
| 1 | MgO | 42.80 | 200 | 0.29 | 2.11 | 32.2 | 11.77 | 0.35 | 4.216 |
| | $Er_2O_3$ | 29.18 | 222 | 0.48 | 3.06 | 18.0 | 20.24 | / | 10.536 |
| 2 | MgO | 42.82 | 200 | 0.24 | 2.11 | 39.0 | 9.70 | 0.29 | 4.214 |
| | $Er_2O_3$ | 29.23 | 222 | 0.28 | 3.05 | 32.2 | 11.80 | / | 10.589 |
| 3 | MgO | 42.90 | 200 | 0.26 | 2.11 | 35.9 | 10.50 | 0.31 | 4.213 |
| | $Er_2O_3$ | 29.32 | 222 | 0.32 | 3.04 | 28.0 | 13.49 | / | 10.585 |

**Table 2** The grain size and band-gap energy values of MgO and Er-doped MgO NPs.

| **MgO samples** | 0 wt. % Er | 1 wt. % Er | 2 wt. % Er | 3 wt. % Er |
|---|---|---|---|---|
| **Grain size from TEM (nm)** | 50 | 47 | 46 | 40 |
| **Cristallites size from XRD (nm)** | 49 | 32 | 39 | 36 |
| **Band-gap energy (eV)** | 5.35 | 5.23 | 5.29 | 5.32 |

**Table 3** Semi-quantitative analysis of EDX measurement of the prepared NPs.

| Samples | Element | Weight (%) | Atomic (%) |
|---|---|---|---|
| Undoped MgO | Mg | 61.59 | 51.48 |
| | O | 38.17 | 48.49 |
| MgO doped 1 % Er | Mg | 61.56 | 52.02 |
| | O | 37.26 | 47.84 |
| | Er | 1.18 | 0.15 |
| MgO doped 2 % Er | Mg | 59.94 | 51.79 |
| | O | 36.36 | 47.74 |
| | Er | 3.70 | 0.46 |
| MgO doped 3 % Er | Mg | 57.06 | 50.09 |
| | O | 36.82 | 49.13 |
| | Er | 6.12 | 0.78 |

**Table 4** A literature overview of MgO photocatalyst doping with different elements (transition metals and rare earth) for the degradation of various organic pollutants from water.

| **Catalyst Synthesis method** | **Doping species Optimal content** | **Crystallite size Shape Band-gap** | **Photocatalytic Conditions Results** | **Refs** |
|---|---|---|---|---|
| MgO and Fe-doped MgO Combustion route | Fe (0.1, 0.5, 1, 2, 3, 4 and 5 mol %) Optimal content = 4 mol % | Decreased from 20 to 12 nm Spherical shape Decreased from 5.4 to 4.9 eV | Pollutant: Methylene blue [MB] = 10 ppm UV light 88% after 120 min | [44] |
| MgO and Ag-doped MgO Sol-gel method | Ag (1, 2, 5, and 7.5 mol %) Optimal content = 2 mol % | Decreased from 12 to 9 nm Agglomerated spherical | Pollutant: Methylene blue [MB] = $10^{-2}$ g $L^{-1}$ UV light = 254 nm 75% after 180 min | [45] |
| MgO and Gd-doped MgO nanoparticles Co-precipitation method | Gd (1, 3, and 5 wt. % Gd Optimal content = 5 wt. % | Decreased from 43 to 27 nm Aggregated sphere Decreased from 3.81 to 3.43 eV | Pollutant: Methylene blue UV light = 365 nm 92% after 160 min | [13] |
| MgO and Ce-doped MgO nanoparticles Wet chemical route (sol-gel) | Ce (1, 2, and 5 mol % Ce Optimal content = 5 mol % | Decreased from 30 to 20 nm Spherical shape Decreased from 3.81 to 3.22 eV | Pollutant: Phenol and CR UV light = 270 and 495 nm 95% for Phenol and 85% for CR after 100 min | [14] |
| MgO and Er-doped MgO nanoparticles Sol-gel method. | Er (1, 2, and 3 wt. %) Optimal content = 3 wt. % | Decreased from 50 to 32 nm Roundish cuboid-shape Between 5.23 to 5.35 eV | Pollutant: Methylene blue [MB] = $10^{-5}$ M UV light = 365 nm 99% after 90 min | Present work |

## References


[1] F. Ciesielczyk, W. Szczekocka, K. Siwińska-Stefańska, A. Piasecki, D. Paukszta, and T. Jesionowski, Evaluation of the photocatalytic ability of a sol-gel-derived MgO-$ZrO_2$ oxide material. Open Chem. 15, 7-18 (2017).

[2] N. Afifah, S. Adriani, N.F. Djaja, and R. Saleh, Photocatalytic degradation of methylene blue and methyl orange with Fe-doped ZnO nanoparticles modified with natural zeolite and montmorillonite: comparative study. Adv. Mater. Res. 1123, 295-302 (2015).

[3] X. Tang, R. Tang, S. Xiong, J. Zheng, L. Li, Z. Zhou, D. Gong, Y. Deng, L. Su, and C. Liao, Application of natural minerals in photocatalytic degradation of organic pollutants: A review. Sci. Total Environ. 812, 152434 (2022).

[4] A. Mahana, S.K. Mehta, Potential of Scenedesmus-fabricated ZnO nanorods in photocatalytic reduction of methylene blue under direct sunlight: kinetics and mechanism. Environ. Sci. Pollut. Res. 28, 28234-28250 (2021).

[5] V. Beena, S. Ajitha, S.L. Rayar,. et al. Enhanced Photocatalytic and Antibacterial Activities of ZnSe Nanoparticles. J. Inorg. Organomet. Polym. Mater. 31, 4390–4401 (2021).

[6] R. Malik, V. K. Tomer, N. Joshi, T. Dankwort, L. Lin, and L. Kienle, Au–$TiO_2$-loaded cubic g-$C_3N_4$ nanohybrids for photocatalytic and volatile organic amine sensing applications. ACS Appl. Mater. Interfaces 40, 34087-34097 (2018).

[7] N. Badar, N. F. Chayed, R. Roshidah, N. Kamarudin, and N. Kamarulzaman, Band gap energies of magnesium oxide nanomaterials synthesized by the sol-gel method. Adv. Mater. Res. 545, 157-160 (2012).

[8] M. R. Anilkumar, H. P. Nagaswarupa, K. S. Anantharaju, K. Gurushantha, C. Pratapkumar, S. C. Prashantha, T. R. Shashishekar et al, Banyan latex: a facile fuel for the multifunctional properties of MgO nanoparticles prepared via auto ignited combustion route. Mater. Res. Express. 2, 095004 (2015).

[9] P. Maiti, P. S. Das, M. Bhattacharya, S. Mukherjee, B. Saha, A. K. Mullick, and A. K. Mukhopadhyay, Transparent $Al^{+3}$ doped MgO thin films for functional applications. Mater. Res. Express. 4, 086405 (2017).

[10] M. Mirhosseini, Evaluation of antibacterial effect of magnesium oxide nanoparticles with nisin and heat in milk. Nanomed. J. 3, 135-142 (2016).

[11] S. Bhatia, N. Verma, and R. K. Bedi, Optical application of Er-doped ZnO nanoparticles for photodegradation of direct red-31 dye. Opt. Mater. 62, 392-398 (2016).

[12] T. AlAbdulaal, M. AlShadidi, M. Hussien, V. Ganesh, A.F. Bouzidi, S. Rafique, H. Algarni, H. Zahran, M. Abdel-Wahab, and I. Yahia, Multifunctional and smart $Er_2O_3$–ZnO nanocomposites for electronic ceramic varistors and visible light degradation of wastewater treatment. Environ. Sci. Pollut. Res. 29, 19109-19131 (2022).

[13] R. V. Shanthi, R. Kayalvizhi, M. J. Abel, and K. Neyvasagam, Optical, structural and photocatalytic properties of rare earth element $Gd^{3+}$ doped MgO nanocrystals. Chem. Phys. Lett. 792, 139384 (2022).

[14] V. T. Srisuvetha, S. L. Rayar, and G. Shanthi, Role of cerium (Ce) dopant on structural, optical and photocatalytic properties of MgO nanoparticles by wet chemical route. J. Mater. Sci.: Mater. Electron. 31, 2799-2808 (2020).

[15] P. K. Labhane, G. H. Sonawane, and S. H. Sonawane, Influence of rare-earth metal on the zinc oxide nanostructures: application in the photocatalytic degradation of methylene blue and p-nitro phenol. Green Process. Synth. 7, 360-371 (2018).

[16] B. Poornaprakash, U. Chalapathi, M. Kumar, K. Subramanyam, S. P. Vattikuti, M. S. P. Reddy, and S. H. Park, Enhanced photocatalytic activity and hydrogen evolution of CdS nanoparticles through Er doping. Ceram. Int. 46, 21728-21735 (2020).

[17] O. Singh, M. Palsingh, N. Kohli and R. Chand singh, Effect of pH on the morphology and gas sensing properties of ZnO nanostructures. Sens. Actuators B Chem. 166-167, 438-443 (2012).

[18] K.D. Salman, H.H. Abbas, and H.A. Aljawad, Synthesis and characterization of MgO nanoparticle via microwave and sol-gel methods. J. Phys. Conf. Ser. 1973, 012104 (2021).

[19] N. Khanna, and A.R. Kumar, Preparation and Characterization of MgO Nanoparticles by Sol-gel Method. Adv. Sci. Lett. 24, 5708-5711 (2018).

[20] X. Zhang, Y. Zheng, H. Yang, Q. Wang, and Z. Zhang, Controlled synthesis of mesocrystal magnesium oxide parallelogram and its catalytic performance. Cryst. Eng. Comm. 17, 2642-2650 (2015).

[21] R. Sathyamoorthy, K. Mageshwari, S. S. Mali, S. Priyadharshini, and P. S. Patil, Effect of organic capping agent on the photocatalytic activity of MgO nanoflakes obtained by thermal decomposition route. Ceram. Int. 39, 323-330 (2013).

[22] W. B. Wang, Y. Yang, A. Yanguas-Gil, N. N. Chang, G. S. Girolami, and J. R. Abelson, Highly conformal magnesium oxide thin films by low-temperature chemical vapor deposition from Mg $(H_3BNMe_2BH_3)_2$ and water. Appl. Phys. Lett. 102, 101605 (2013).

[23] M.A. Alavi, and A. Morsali, Syntheses and characterization of Mg $(OH)_2$ and MgO nanostructures by ultrasonic method. Ultrason Sonochem. 17, 441-446 (2010).

[24] Z.X. Tang, and L.E. Shi, Preparation of nano-MgO using ultrasonic method and its characteristics.Eclet.Quim.33, 15-20 (2008).

[25] K.D. Bhatte, D.N. Sawant, K.M. Deshmukh, and B.M. Bhanage, Additive free microwave assisted synthesis of nanocrystalline Mg $(OH)_2$ and MgO. Particuology. 10, 384-387 (2012).

[26] T.H. Duong, T.N. Nguyen, H.T. Oanh. et al., Synthesis of Magnesium Oxide Nanoplates and Their Application in Nitrogen Dioxide and Sulfur Dioxide Adsorption. J. Chem. (2119).

[27] S.K. Moorthy, C. H. Ashok, K. VenkateswaraRao, and C. Viswanathan, Synthesis and characterization of MgO nanoparticles by Neem leaves through green method. Mater. Today: Proc. 2, 4360-4368 (2015).

[28] J. Suresh, R. Yuvakkumar, M. Sundrarajan, and S.Ig.Hong, Green synthesis of magnesium oxide nanoparticles. Adv. Mater. Res. 952, 141-144 (2014).

[29] M. Mohsen, H. Tantawy, I. Naeem, M. Awaad, O. Abuzalat, and A. Baraka, Activation of Cadmium–Imidazole Buffering Coordination Polymer by Sulfur-Doping for the Enhancement of Photocatalytic Degradation of Cationic and Anionic Dyes Under Visible Light. J. Inorg. Organomet. Polym. Mater. 1-14 (2022).

[30] I. Ameur, B. Boudine, M. Laidoudi, M. Khennoucha, V. Brien, D. Horwat, M. Sebais, and O. Halimi, Influence of magnesium doping on microstructure, optical and photocatalytic activity of zinc oxide thin films synthesis by sol–gel route. Appl. Phys. A. 127, 1-14 (2021).

[31] B. Rahal, B. Boudine, Y. Larbah. et al, Influence of Low Cd-Doping Concentration (0.5 and 3 wt.%) and Different Substrate Types (Glass and Silicon) on the Properties of Dip Coated Nanostructured ZnO Semiconductors Thin Films. J. Inorg. Organomet. Polym. Mater. 31, 4001–4017 (2021).

[32] P. B. Devaraja, D. N. Avadhani, H. Nagabhushana, S. C. Prashantha, S. C. Sharma, B. M. Nagabhushana, H. P. Nagaswarupa, and B. D. Prasad, Luminescence properties of MgO: $Fe^{3+}$ nanopowders for WLEDs under NUV excitation prepared via propellant combustion route. J. Radiat. Res. Appl. Sci. 8, 362-373 (2015).

[33] L.X. Li, D. Xu, X. Q. Li, W.C. Liu, and Y. Jia, Excellent fluoride removal properties of porous hollow MgO microspheres. New J Chem. 38, 5445-5452 (2014).

[34] B. Saravanakumar, S. Muthulakshmi, G. Ravi, V. Ganesh, A. Sakunthala, and R. Yuvakkumar, Surfactant effect on synthesis and electrochemical properties of nickel-doped magnesium oxide (Ni–MgO) for supercapacitor applications. Appl. Phys. A. 123, 1-9 (2017).

[35] S. Kianipour, F. S. Razavi, M. Hajizadeh-Oghaz, W. K. Abdulsahib, M. A. Mahdi, L. S. Jasim, and M. Salavati-Niasari, The synthesis of the P/N-type $NdCoO_3$/g-$C_3N_4$ nano-

heterojunction as a high-performance photocatalyst for the enhanced photocatalytic degradation of pollutants under visible-light irradiation. Arab. J. Chem. 15, 103840 (2022).

[36] S. R. Yousefi, M. Ghanbari, O. Amiri, Z. Marzhoseyni, P. Mehdizadeh, M. Hajizadeh-Oghaz, and M. Salavati-Niasari, $Dy_2BaCuO_5/Ba_4DyCu_3O_{9.09}$ S-scheme heterojunction nanocomposite with enhanced photocatalytic and antibacterial activities. J. Am. Ceram. Soc. 104, 2952-2965 (2021).

[37] H. Ali, and A. M. Ismail, Honeycomb-like $V_2O_5$ Based Films: Synthesis, Structural, Thermal, and Optical Properties for Environmental Applications. J. Inorg. Organomet. Polym. Mater. 1-18 (2022).

[38] R. Boulkroune, M. Sebais, Y. Messai, R. Bourzami, M. Schmutz, C. Blanck, O. Halimi, and B. Boudine, Hydrothermal synthesis of strontium-doped ZnS nanoparticles: structural, electronic and photocatalytic investigations. Bull. Mater. Sci. 42, 1-8 (2019).

[39] L. Cheng, Q. Xiang, Y. Liao, and H. Zhang, CdS-based photocatalysts. Energy Environ. Sci. 11, 1362-1391 (2018).

[40] Y. Zheng et al, Microscale flower-like magnesium oxide for highly efficient photocatalytic degradation of organic dyes in aqueous solution. RSC adv. 9, 7338-7348 (2019).

[41] K. Mageshwari, S. S. Mali, R. Sathyamoorthy, and P. S. Patil, Template-free synthesis of MgO nanoparticles for effective photocatalytic applications. Powder technol. 249, 456-462 (2013).

[42] M. R. Islam, M. Rahman, S. F. U. Farhad, and J. Podder, Structural, optical and photocatalysis properties of sol–gel deposited Al-doped ZnO thin films. Surf. Interfaces. 16, 120-126 (2019).

[43] S. Klubnuan, P. Amornpitoksuk, and S. Suwanboon, Structural, optical and photocatalytic properties of MgO/ZnO nanocomposites prepared by a hydrothermal method. Mater. Sci. Semicond. Process. 39, 515-520 (2015).

[44] M. R. Anilkumar, H. P. Nagaswarupa, H. Nagabhushana, S. C. Sharma, Y. S. Vidya, K. S. Anantharaju, S. C. Prashantha, C. Shivakuamra, and K. Gurushantha, Bio-inspired route for the synthesis of spherical shaped MgO: $Fe^{3+}$ nanoparticles: Structural, photoluminescence and photocatalytic investigation. Spectrochim. Acta A: Mol. Biomol. Spectrosc. 149, 703-713 (2015).

[45] Z. M. Alaizeri, H. A. Alhadlaq, S. Aldawood, M. J. Akhtar, M. S. Amer, and M. Ahamed, Facile synthesis, characterization, photocatalytic activity, and cytotoxicity of Ag-doped MgO nanoparticles. Nanomaterials 11, 2915 (2021).

**Declarations:**

**Funding info**: The authors have no relevant financial or non-financial interests to disclose.

**Competing interests**: The authors have no conflicts of interest to declare that are relevant to the content of this article.

**Author contribution**: All authors conceived and designed the study. Imene Ameur conducted the experiments. All authors contributed to manuscript revisions. All authors approved the final version of the manuscript and agree to be held accountable for the content therein.

Conceptualization: Boubekeur BOUDINE and Imene AMEUR; Methodology: Boubekeur BOUDINE and Imene AMEUR; Formal analysis and investigation: All authors; Writing-original draft preparation: All authors; Writing - review and editing: All authors; Funding acquisition: All authors; Resources: All authors; Supervision: Boubekeur BOUDINE.

**Availability of data and materials**: Not applicable

**Code availability**: Not applicable.